

3.2 Machine physics

3.2.1 Beam Injection

The accelerated beam from the booster is injected into the main storage ring. The output current from the booster is given by the demand to fill the CANDLE storage ring within one minute to the mean current of 350 mA. Taking into account the booster synchrotron repetition rate of 2 Hz and the particle revolution time of 720 ns in storage ring the output current from the booster should be

$$I = \frac{350mA \cdot 720nsec}{60sec \cdot 2sec^{-1} \cdot 500nsec} = 4.2mA \quad (3.2.1)$$

Considering some losses in the whole injection chain, the linac output current of 10-15 mA will be more than sufficient. The injection scheme is the straightforward multi-turn injection. The ring acceptance is bumped so that the part of the acceptance is spaced out of the injection septum where the incoming beam from booster is injected. After the proper injection of the beam pulse the bump is switched off and the coherent oscillations of the injected beam are damped in successive number of turns due to radiation damping of oscillations. After a few damping times (storage ring horizontal radiation damping time is 3.8 ms) the beam bump switches on and the next pulse from the booster can be injected. The components of the transfer line between the booster and storage ring that includes the last septum are adjusted for exact matching of the geometrical and optical parameters of the incoming beam with storage ring lattice parameters. The injection is performed in a horizontal plane and the matching at the septum output is done for transverse amplitude functions α, β and horizontal dispersion functions η, η' .

In the preliminary version, the injection scheme with the arrangement of septum magnets in one of long straight section and with kickers locations between two sextupoles in neighbor arc sections was studied in detail. The main disadvantages of this option are the complicated and unbalanced closed orbit bump amplitude due to non-linearities of sextupole fields. The optimization of the injection bump leads to a scheme with four kicker magnets located in one long straight section of the storage ring. Although this option implies relatively strong kicker field, the clear advantage is that created bump is independent of the values of beta function at the injection point. Injection into the storage ring takes place in a long straight section from the internal side of the storage ring, in horizontal phase space.

Fig. 3.2.1 shows schematically the injection system and the bumped orbit. Four bump magnets produce a closed bump with the deflection of 12 mm at the septum output. The injection thin septum (septum thickness is 2mm) is located at the distance of 14 mm from the reference orbit thus 10 mm of horizontal acceptance is available for the capture of the injected beam.

Two septum magnets, a thin with deflection angle of 3° and a thicker one with deflection angle of 8° are used to produce the final deflection of the incoming beam from booster to the machine bumped closed orbit. The comparatively large deflection angle of thick septum is chosen to keep the beam pipe far from the nearest kicker, as well as to allow comfortable disposition of the third dipole magnet in booster-to-storage ring transfer line. The length of storage ring straight section is 4.8 m. The bump magnets are capable of displacing the orbit by up to 12 mm. This orbit offset corresponds to the kick angle about 12 mrad for each bump magnet. The radial position of the thin injection septum is

adjustable in order to produce the best match to the dynamic aperture. Table 3.2.1 lists the main characteristics of the injection system.

Table 3.2.1 Storage ring injection parameters.

Energy (GeV)	3
Stored beam emittance ($nm \cdot rad$)	8.4
Injected beam emittance ($nm \cdot rad$)	74.9
Injected beam number of sigmas	3
Distance of injected beam to septum (mm)	3
Beta at injection point (m)	7.89
Effective septum thickness (mm)	3
Orbit displacement at septum (mm)	12

An extracted from the booster electron beam has the horizontal emittance of $75 nm \cdot rad$ and the rms energy spread of $6.7 \cdot 10^{-4}$. The electron beam delivered by booster-to-storage ring (BTS) transfer line has the transverse dimensions of 2.4mm in horizontal and 0.3mm in vertical planes for 3σ beam size at the entrance of injection thick septum. This compensates the most stringent demands on storage ring injection scheme coming from the relatively short length of straight section and dense arrangement of injection elements.

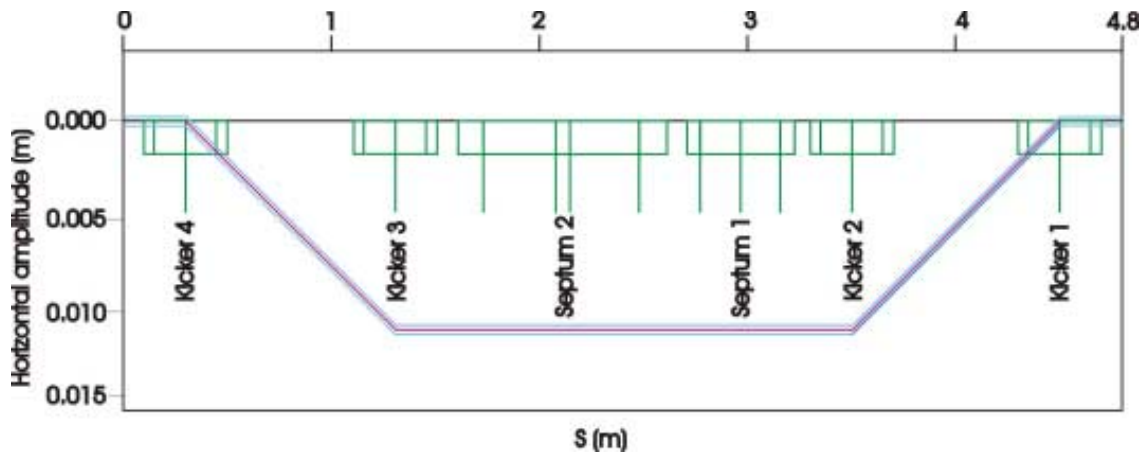


Fig.3.2.1 The scheme of injection system and bumped orbit.

The horizontal half-aperture needed to accommodate injection is 22 mm, while the half aperture of vacuum chamber is 37 mm. To correctly estimate the injection acceptance, the booster horizontal beam size has been taken at 3σ and 1% coupling. 3 mm effective septum thickness has been used to take into account power supply jitter and misalignments. The reduction of horizontal aperture by the septum magnet results in $13 mm \cdot mrad$ of dynamic acceptance that, in turn, limits the momentum acceptance by about 3.2%. The Touschek lifetime strongly depends on the momentum acceptance of the lattice, which can be limited either longitudinally (by the RF or dynamic acceptance) or transversely (by the physical or the dynamic acceptance). For CANDLE storage ring lattice the limit on momentum acceptance set by RF is of the order of 2.4%. Thus, there is no real loss in beam Touschek lifetime due to reduction of dynamic acceptance caused by septum position.

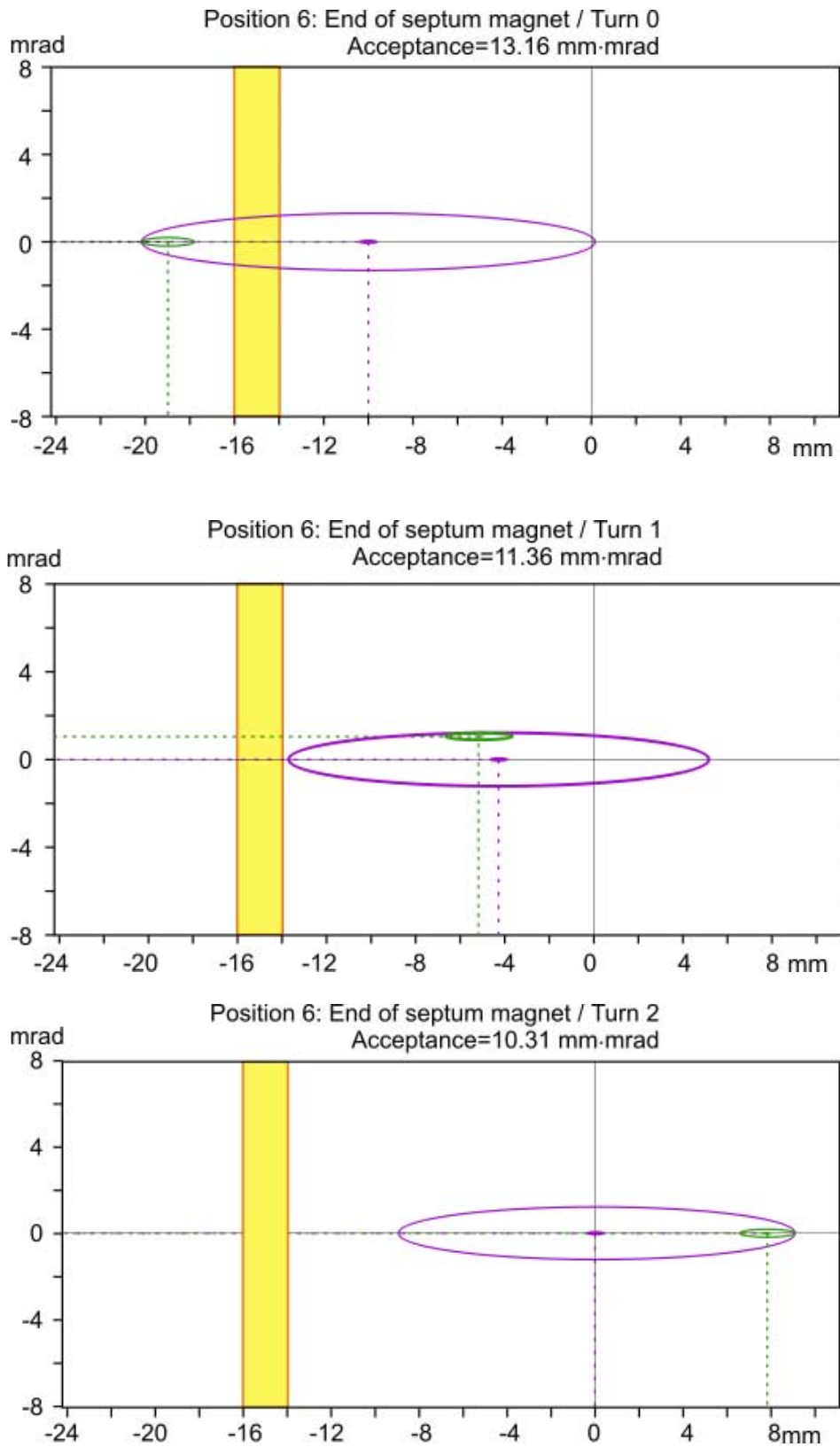


Fig. 3.2.2 The bumped acceptance, stored and injected beams. Shown are the dynamics at the injection start, after the first and the second turns in the storage ring.

Figure 3.2.2 (top) shows the positions of closed orbit and the injected beam at the output of the septum magnet. It can be seen that the injected beam fits well within the acceptance of the ring. The evolution of the bumped acceptance and the injected beam coherent oscillations after one and two turns is shown in Fig. 3.2.2 (bottom). The kicker magnet field rise time is set $2\ \mu s$, which is less than three beam turns in the ring (the revolution time is $0.72\ \mu s$). The bump magnets are then turned off in a time corresponding to about three orbits of the ring to prevent the injected particle loss due to colliding with the septum. Thus, the injection scheme is capable of operating both in single-turn and in multi-turn regime. The newly injected beam then undergoes coherent betatron motion about the closed orbit- motion that is rapidly damped by means of synchrotron radiation with damping time of 3.8 ms. This process is repeated at the booster cycle rate of 2Hz until the desired beam current of 350mA is stored in the storage ring.

The main parameters of bump magnets and injection septa are summarized in Table 3.2.2. The detailed description of the injection system magnets is given in Section 3.7.

Table 3.2.2 Main parameters of storage ring injection magnets.

	Thick septum	Thin septum	Bump magnets
Length, (m)	1.2	0.5	0.4
Bend angle (deg)	8	3	0.687
Magnetic field (T)	1.14	1.01	0.3
Rise/Fall time	half-sine $100\ \mu s$	half-sine $30\ \mu s$	half-sine $2\ \mu s$

3.2.2 Misalignment and Field Errors

Third-generation light sources are characterized by an increased emphasis on the quality of the emitted photon beam, expressed in terms of its spectral brightness. High photon brightness implies a low emittance of electron beam. In order to achieve low emittance the dispersion and horizontal beta function at the bending magnet location must be small, which means the use of strong focusing optics. Strong focusing optics, in turn, requires strong chromaticity correction sextupoles and increase sensitivity to quadrupole misalignment and movement. Another aspect of limitations arises from the user demands on long time photon beam orbit stability at the level of less than 10% of photon beam spot size. This requirement is especially stringent in the vertical plane, where the source size is very small. All these effects lead to very small tolerances with a fraction of millimeter as a closed orbit error. It is obvious that in third-generation light sources the magnetic lattice design needs more careful alignment, stabilization and corrections.

In real machines the closed orbit results not only from the ideal magnet lattice but also from field errors arising from magnetic element positioning errors. The magnetic elements can be positioned only with a finite alignment precision of about 0.1 mm. Even if one could align the magnetic elements precisely on the ideal closed orbit, this position would change with time due to ground movements and vibrations. The most severe effects comes from the misalignment of quadrupole magnets, where the resulting error dipole field is proportional to both gradient and alignment error.

The components in iron-dominated magnets arise because the poles have finite dimensions to accommodate the excitation windings and are constructed using finite tolerances. The first constraint leads to systematic multipole components (the same in all magnets of the

same type), the second leads to both normal and skew components with random amplitudes. Random multiple errors are introduced by magnet assembly imperfections that vary from magnet to magnet. The main effect of multiple field errors in case of unperturbed machine is the reduction of dynamic aperture.

The sensitivity of the CANDLE storage ring magnetic system to alignment errors has been investigated using the program MAD [1]. The systematic field errors for storage ring magnets as computed by the program POISON [2] are presented in Table 3.2.3.

Table 3.2.3 Systematic multiple field components

Magnet	Multiple order	Radius (mm)	$\Delta B_n / B$
Dipole	2	22	1.0×10^{-4}
Quadrupole	6	32.5	3.2×10^{-4}
Quadrupole	10	32.5	3.8×10^{-4}
Quadrupole	14	32.5	1.0×10^{-3}
Sextupole	9	30	3.5×10^{-3}
Sextupole	15	30	1.5×10^{-3}

The random components coming from construction tolerances are different for each magnet and are present in principle at all orders. Table 3.2.4 lists the multiple components and their rms strengths, which are considered the most likely to occur actually.

Table 3.2.4 Random multiple field errors

Multiple order	Dipole, $\Delta B_n / B$	Quadrupole, $\Delta G_n / G$
1	10^{-5}	10^{-5}
2	10^{-4}	10^{-5}
3	10^{-5}	10^{-5}
4	10^{-5}	10^{-5}
5	0.0	10^{-5}
9	0.0	10^{-7}

The results of tracking simulations are shown in Fig 3.2.3 and Fig 3.2.4. Fig 3.2.3 presents the dynamic aperture in the presence of multipole errors. It is seen that the main effect of the errors is observed in the radial plane, where the aperture was reduced from 23 mm to 15mm. This value of dynamic aperture is quite sufficient both for injection and for an acceptable beam lifetime. The analysis of dynamic aperture sensitivity to a particular multipole component shows that the random gradient error in the dipole magnet is the most harmful component.

Fig 3.2.4 shows the dynamic aperture of unperturbed machine in comparison with the presence of misalignments before and after the correction, respectively. We found that after the correction, no essential dynamic aperture reduction is observed with alignment errors at the level of 0.1 mm.

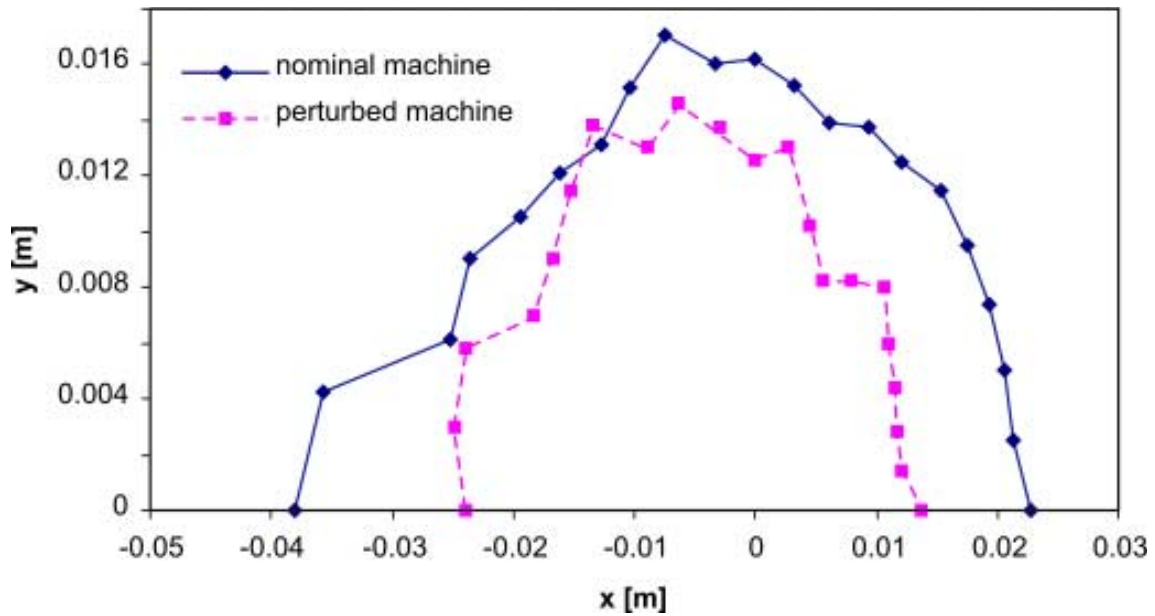


Fig 3.2.3 Dynamic aperture reduction due to random multiple errors.

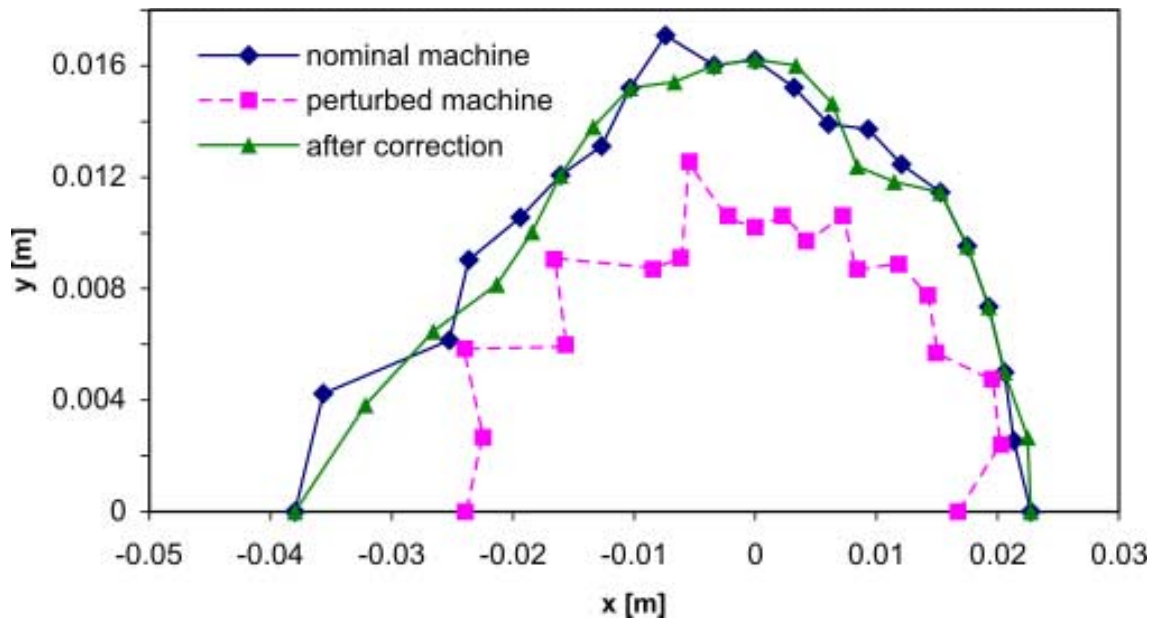


Fig.3.2.4 Dynamic apertures of the ring: ideal, misaligned and corrected.

To study the effects of magnet misalignments, errors were randomly distributed around the storage ring lattice and the statistics was compiled for the closed orbit distortions. Typical examples of closed orbit distortion (COD) for the horizontal and vertical planes are shown in Fig.3.2.5 and Fig 3.2.6 respectively.

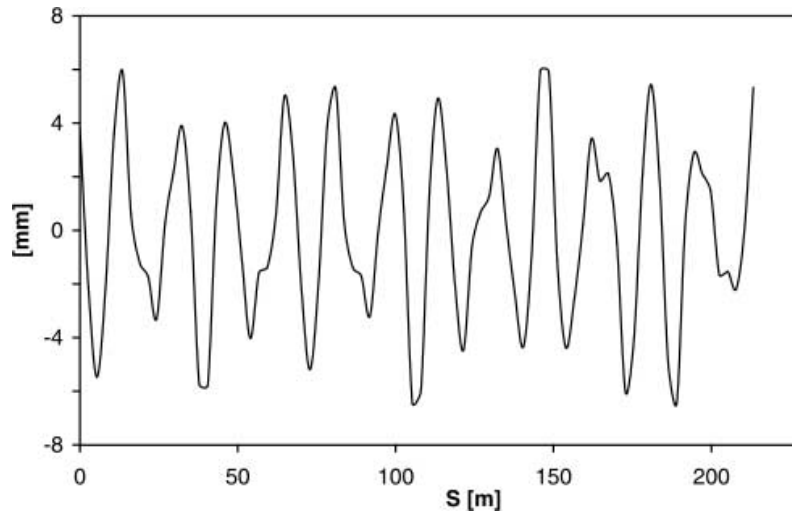


Fig.3.2.5 Horizontal COD due to random magnet errors (before correction).

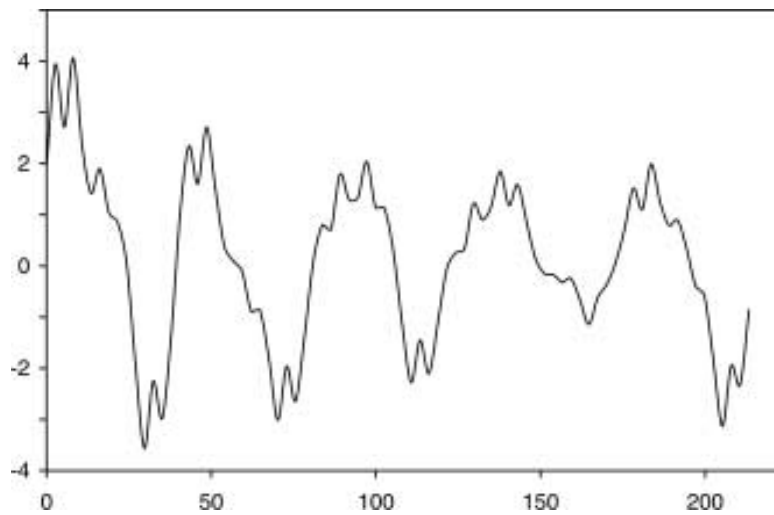


Fig.3.2.6 Vertical COD due to random magnet errors (before correction).

Single orbit can have local displacement of up to 6 mm in horizontal plane and 4 mm in vertical plane. The expectation value for the closed orbit rms distortion in horizontal and vertical planes are 2.7 mm and 2.1 mm respectively (see Fig.3.2.7).

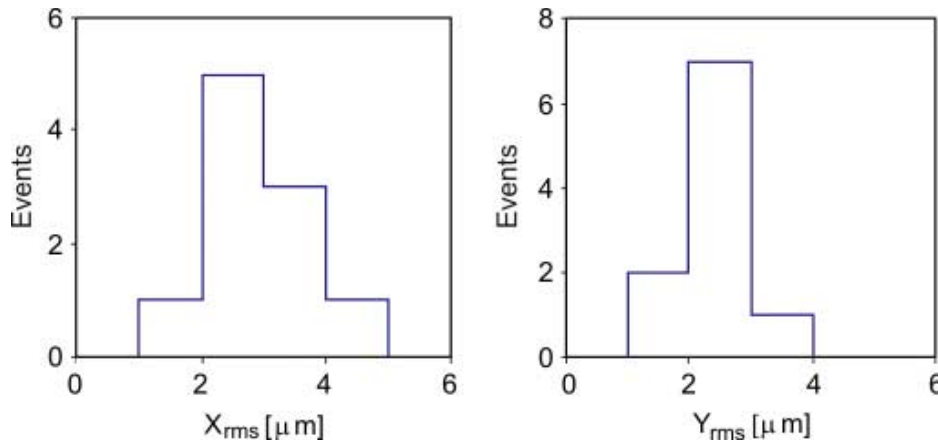


Fig.3.2.7 The rms COD produced by ten sets of random errors before correction.

Since the exact alignment position of each magnet is not known, it has become normal practice to describe the problem with using the statistical method. The computed amplitude of the average closed orbit with the amplification factor of about 26 is in good agreement with these that estimated using the standard formula for random distribution of quadrupole displacements with an rms value σ_u [3]:

$$\langle u_0^2(s) \rangle^{1/2} = \beta(s)^{1/2} \cdot A \cdot \sigma_u, \quad (3.2.2)$$

where the error amplification factor is defined by

$$A^2 = \frac{N}{8 \cdot \sin^2 \pi \nu} \langle (k \cdot l)^2 \cdot \beta_k \rangle \quad (3.2.3)$$

Here $u_0(s)$ is the expectation value for the orbit distortion, $\beta(s)$ is the beta function at observation point, σ_u is the standard rms deviation of errors; k is the quadrupole strength, l is the quadrupole length, β_k is the beta function in the quadrupoles, N is the number of magnets in quadrupole family.

3.2.3 Closed Orbit Correction

Closed orbit distortions (COD) are generated mainly by quadrupole displacement errors and dipole field errors. In estimating the COD, we have taken alignment tolerances and field errors presented in the Table 3.2.5. The simulation of ten sets of the alignment errors has been carried out under the assumption of Gaussian distributions of errors with rms values given in Table 3.2.5. The truncation error of 2.5σ was used in tracking simulations. Since the combined function dipole magnet with quadrupole field is adopted for CANDLE lattice, the dipole alignment tolerances are taken of the same order as the ones used for quadrupoles.

Table 3.2.5 Local magnet alignment tolerances.

Magnet	Dipole	Quadrupole	Sextupole
Horizontal rms displacement (mm)	0.1	0.1	0.1
Vertical rms displacement (mm)	0.1	0.1	0.1
Tilt rms angle (mrad)	0.5	0.5	0.5

Closed orbit tracking simulations and correction procedure were done using the program MAD [1], where the correction is performed by subroutine program MICADO [4] using an iterative method based on the least square minimization theory.

The disturbed closed orbit has been calculated and “measured” by 80 beam position monitors (BPM) distributed around the storage ring (Fig. 3.2.8).

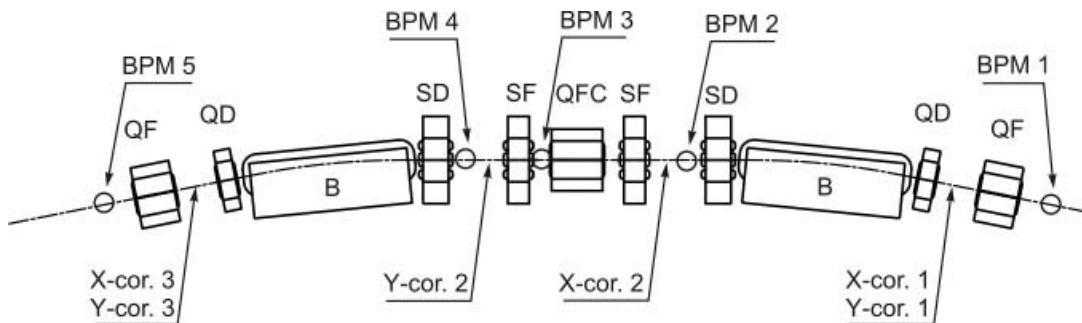


Fig 3.2.8 BPMs and correctors distribution per magnetic cell.

The BPMs are placed at the crucial points close to the quadrupoles and sextupoles, where misalignments serve as sources for orbit distortion and dynamic aperture reduction, and at the end of each insertion straight section in order to provide local closed orbit adjustment. Distributions of the corresponding rms values of the orbit distortions after the correction are shown in Fig.3.2.9. The most efficient correction is obtained when the correctors are located as close as possible to the sources generating the largest orbit deviation, i.e. the quadrupoles.

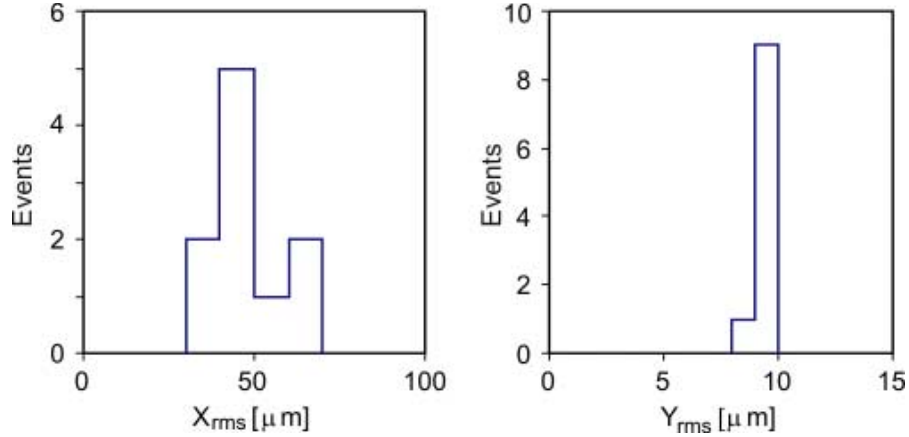


Fig.3.2.9 Calculated rms closed orbit distortion produced by ten sets of random errors (after correction).

The storage ring has 64 corrector magnets in total: 32 with combined function for correction in both horizontal and vertical planes, 16 horizontal and 16 vertical correctors. Their arrangement over one period of the lattice is shown in Fig. 3.2.8. The combined function corrector strengths for one typical random set of quadrupole alignment are presented in Table 3.2.6. The beta functions in the location of the correctors are $\beta_x = 6.9\text{m}$ and $\beta_y = 7.2\text{m}$ respectively.

Table 3.2.6 Combined function corrector strengths.

Corrector	Position (m)	Hor.correct. (mrad)	Vert.Correct. (mrad)	Corrector	Position (m)	Hor. orrect. (mrad)	Vert.Correct. (mrad)
KHV1	2.78	0.073011	-0.03048	KHV17	110.78	-0.08235	0.066597
KHV2	10.72	-0.01342	0.128725	KHV18	118.72	-0.03124	-0.08468
KHV3	16.28	-0.06589	-0.02105	KHV19	124.28	-0.07247	0.03859
KHV4	24.22	-0.06005	-0.01763	KHV20	132.22	-0.07399	-0.04444
KHV5	29.78	-0.1643	-0.04434	KHV21	137.78	-0.12601	0.182954
KHV6	37.72	-0.09436	-0.08575	KHV22	145.72	-0.03217	-0.00195
KHV7	43.28	0.055827	-0.03046	KHV23	151.28	-0.02	-0.17885
KHV8	51.22	0.023113	0.009324	KHV24	159.22	-0.02486	-0.07861
KHV9	56.78	-0.00199	-0.07109	KHV25	164.78	-0.11795	-0.00499
KHV10	64.72	-0.1391	-0.02511	KHV26	172.72	-0.11753	0.110748
KHV11	70.28	-0.05856	-0.06396	KHV27	178.28	0.081448	0.086518
KHV12	78.22	-0.03746	-0.03409	KHV28	186.22	-0.06893	0.099246
KHV13	83.78	-0.04849	-0.00403	KHV29	191.78	0.128714	0.045241
KHV14	91.72	-0.15947	-0.00201	KHV30	199.72	-0.09226	-0.1263
KHV15	97.28	-0.01711	0.069763	KHV31	205.28	0.133158	0.029819
KHV16	105.22	-0.00352	0.052999	KHV32	213.22	-0.15518	0.057684

Fig. 3.2.10 and Fig. 3.2.11 show the results of closed orbit correction for one particular set of errors with the BPM's rms misalignment of 0.1 mm. Since the rms momentum spread in the beam is of 10^{-4} order, the resulting increase in beam size of $4 \mu\text{m}$ is negligibly small in comparison with the natural beam rms size.

The overall correction method gives good results in both planes by letting the rms closed orbit to be reduced by factor of about 30 with corrector strengths that are easily obtained by means of combined function horizontal/vertical correctors. Given results were achieved after the 2-3 iterations using possible small amount of correctors.

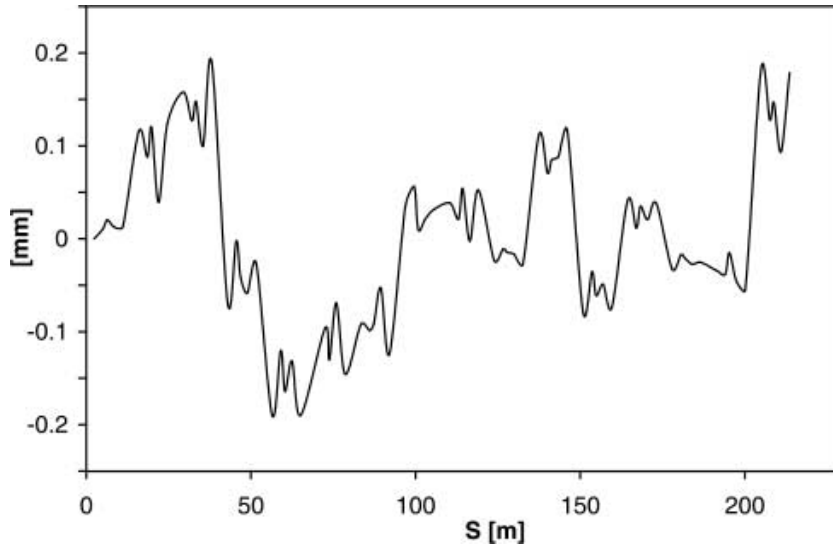


Fig. 3.2.10 Horizontal closed orbit residual distortion after correction.

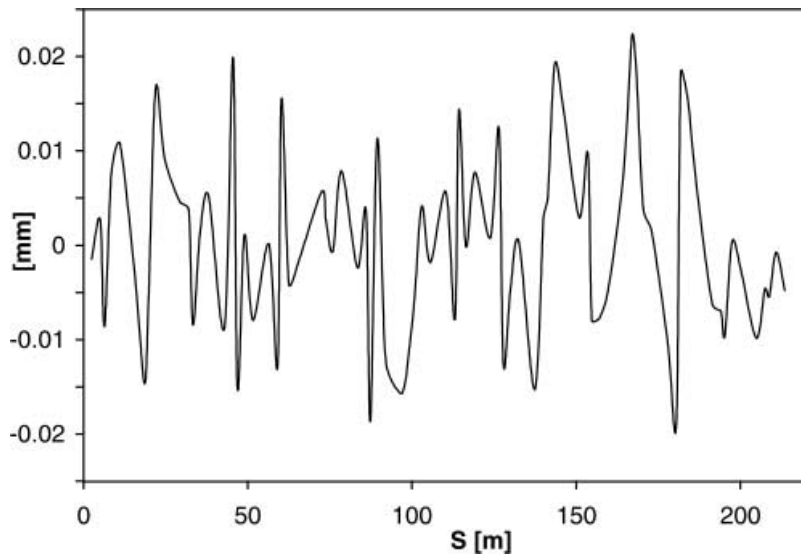


Fig. 3.2.11 Vertical closed orbit residual distortion after correction.

3.2.4 Coupling and Correction

The vertical beam size in the storage ring is determined by the coupling of horizontal betatron oscillations and by vertical dispersion. The coupling is generated due to quadrupole magnet roll misalignments and due to vertical closed orbit offset with the magnetic center of sextupoles. Vertical bending, which causes vertical dispersion, arises from the dipole roll, vertical quadrupole displacement and vertical orbit steering magnets.

As it was mentioned above, one cell of magnetic lattice will contain five BPMs and four corrector magnets, two of which are of combined type for focusing in both transverse planes, resulting in three correctors per cell for each plane. The corrector magnets will be installed between the doublet quadrupoles and between the sextupole magnets in dispersion section, where there is enough space for their installation.

The CANDLE orbit control system will be based on a singular value decomposition (SVD) control algorithm. This system produces reliable global orbit correction, local orbit adjustments and photon beam steering. In our simulations for coupled optics we use the Matlab based accelerator toolbox AT [5], which provides a wide range of high-level simulation options ranging from 6-D symplectic tracking to perform the calculations of closed orbit and coupled optics. In AT the coupled optic simulation is based on the formalism [6,7] of decomposition of full-turn transfer matrix in the form:

$$T = V \cdot U \cdot V^{-1} \quad (3.2.4)$$

$$U = \begin{bmatrix} A & 0 \\ 0 & B \end{bmatrix}; \quad V = \begin{bmatrix} \gamma \cdot I & C \\ -C^+ & \gamma \cdot I \end{bmatrix} \quad (3.2.5)$$

where matrixes A and B are interpreted as the Twiss matrixes of normal modes and the matrix C describes the coupling. For weak coupling systems the elements of coupling matrix C and mixing parameter γ characterize the coupling of horizontal and vertical motions so that the coupling coefficient can be approximately presented as

$$k = 2 \cdot \left\langle \frac{C_{12}^2}{\beta_x \cdot \beta_y} \right\rangle \quad (3.2.6)$$

where one has to take averaging over the ring. Fig. 3.2.12 gives the evaluation of elements of coupling matrix along the storage ring. The coupling is generated by the quadrupoles with the tilt random rms errors of 0.5 mrad.

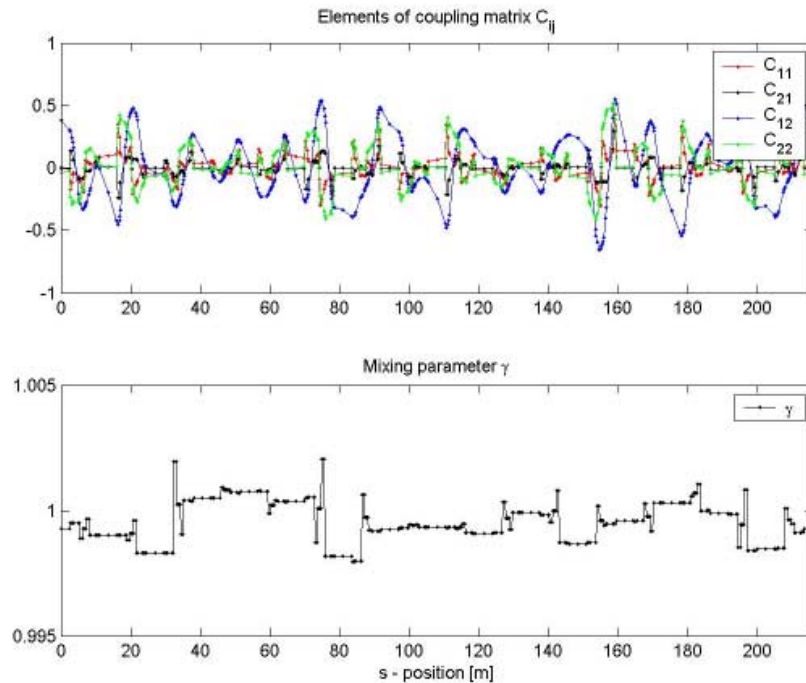


Fig. 3.2.12 Elements of coupling matrix (top) and mixing parameter.

Putting approximately $\beta_x \cdot \beta_y \approx 36$ and taking into account Fig.3.2.12, the coupling coefficient is estimated at the level of $k \approx 1.6\%$. This value is quite acceptable to keep the optimum machine operation performances and does not require special coupling correction scheme. However, additional dipole windings are foreseen in some of sextupoles, which will be used for fine-tuning of the orbit at the insertion devices.

The orbit response matrix measures the change in the transverse orbit position caused by a transverse kick. The response matrix can be measured in a real machine or computed with an accelerator code. A popular technique for linear optics determination fits the parameters in the model, such as K-values of quadrupoles, corrector gains, and BPM errors, to minimize the difference between the measured and the model response matrix. Program AT uses easily Matlab's capability of matrix manipulation to solve SVD problem for parameter fitting. The response matrix in AT is represented in the form:

$$R = \begin{pmatrix} HH & HV \\ VH & VV \end{pmatrix}; \quad (3.2.7)$$

where HH is the horizontal BPM response to horizontal orbit kick, HV is the horizontal BPM response to vertical orbit kick, VH is vertical BPM response to horizontal orbit kick, VV is the vertical BPM response to vertical orbit kick. The response matrixes are shown in Fig.3.2.13a-c: a) for the ideal machine (without coupling), b) in case of weak coupling generated by magnets random misalignments with the rms random error 0.1mm and c) in case of coupling caused by inclusion of the random tilts in all quadrupole families with rms value of 0.5 mrad.

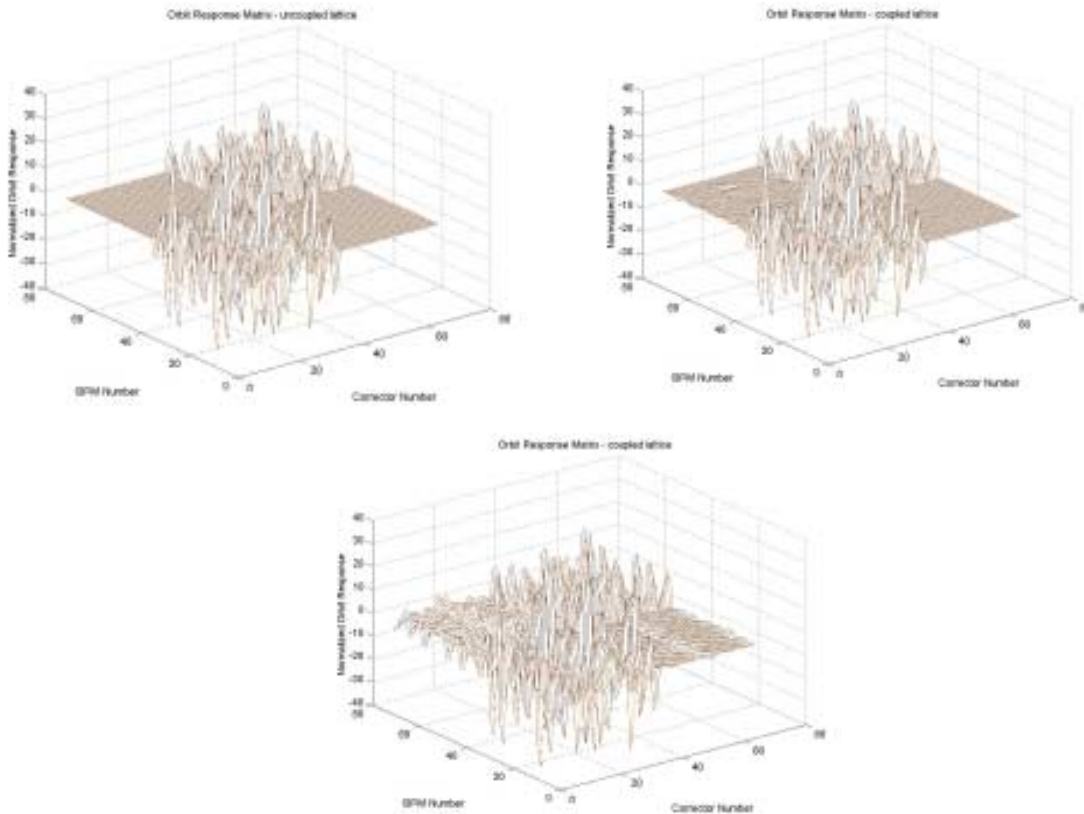


Fig. 3.2.13 Storage ring response matrix in case of a) ideal machine, b) weak coupling and c) including quadrupole tilt errors.

In the figure the normalized closed orbit distortion $\Delta x / \Delta \sigma$ is depicted in the vertical axis with Δx the absolute closed orbit distortion and $\Delta \sigma$ the value of misalignment error. Recent advances in developing an interactive orbit control program at SSRL [8], the usage of Matlab for orbit control applications in storage rings take advantage of easy-to-use mathematical and graphics routines of Matlab and makes more promising. We are going to widely implement this technique in CANDLE machine control and diagnostic system.

3.2.5 Effects of Insertion Devices

Optical effects.

Insertion devices are the indispensable part of third generation light sources. With the installation of insertion devices (ID's) into the ring one expects to observe three main classes of perturbations to the beam:

- closed orbit distortion;
- tune shifts and betatron beat;
- reduction of dynamic aperture.

The closed orbit distortion is induced by the field and positioning errors of the magnets. A modern technology of proper shimming and high precision alignment ensure a negligible closed orbit distortion due to installation of insertion devices. In this concern the basic requirement of an ID is that the beam will return to its nominal orbit after passing through the insertion device. In the first order, taking the field distribution symmetric around the device midpoint and adjusting the integral field to zero fulfill this requirement, so

$$\int_{-l/2}^{l/2} B_y(s) ds = 0 ; \quad B_y(x, y, s) = B_y(x, y, -s). \quad (3.2.8)$$

Usually it is achieved by equipping the ID with reduced field or reduced length end poles of the same type like the central ones.

In general the perturbations induced by the presence of insertion devices may be divided into two classes. Firstly there are effects coming from magnetic field influence resulting in distortion of the linear optics, tune shifts, excitation of resonance's, reduction of the dynamic aperture. The second group of insertion devices effects are connected with the beam emitted radiation in the ID, which cause changes in the emittance and energy spread of the beam. Most of the effects of IDs are detrimental to the machine performance and must be compensated. But in some cases the radiation effects can be used as an advantage for emittance reduction.

The present CANDLE lattice design consists of 16 identical straight sections 12 of which are available for IDs. Each straight section has 4.8 m length with 4m available for the installation of ID. Because the CANDLE beam emittance is larger than the diffraction limited emittance for the expected photon wavelength range, we find the lattice optical functions in the middle of straight section to be optimal with horizontal beta 7.9 m and vertical beta 4.87m that provide a good performance for both machine reliability and high spectral brightness of the radiated photon [9].

The primary CANDLE beamlines will be based on conventional permanent magnet planar insertion devices [10]. In Table 3.2.7 the basic parameters of primary insertion devices are

summarized. There is a conventional planar wiggler and two undulators incorporated in the lattice design to cover the radiated photon spectrum in the range of 0.1 - 30 keV. Such devices with very similar parameters are widely used in many SR world centers with good performance and reliable operation [11, 12]. All three devices have conventional in-air gap permanent magnet structure.

Table 3.2.7 CANDLE insertion devices parameters

Insertion Devices	Wiggler I	Undulator I	Undulator II
Period length, m	0.17	0.022	0.05
Number of periods	23	72	79
Magnetic field, T	1.98	0.7	0.3
K-value	32	1.43	1.4
Gap height, mm	18	5.6	24

In this section we present the results of linear effects of these IDs on electron beam parameters and storage ring optics based on the analytical approach developed in [13]. The studies of the influence of ID on beam dynamic aperture and tracking simulations were done with the computer code OPA [14].

The components of the insertion device magnetic field used for the derivation of equation of motion are as follows:

$$\begin{aligned}
 B_x &= (k_x / k_y) B_0 \sinh(k_x x) \sinh(k_y y) \cos(ks); \\
 B_y &= B_0 \cosh(k_x x) \cosh(k_y y) \cos(ks); \\
 B_z &= -(k / k_y) B_0 \cosh(k_x x) \sinh(k_y y) \sin(ks);
 \end{aligned}
 \tag{3.2.9}$$

with

$$k_x^2 + k_y^2 = k^2 = \left(\frac{2\pi}{\lambda}\right)^2; \tag{3.2.10}$$

where λ is the period length of the ID and B_0 is its peak magnetic field. The equation of motion contains a linear term, the effect of which is equivalent to that of horizontally and vertically focusing quadrupole whose strengths are given by:

$$K_{Q_{x,y}} = \frac{1}{2} \left(\frac{k_{x,y}}{\rho k} \right)^2 \tag{3.2.11}$$

For the chosen planar insertion devices $k_x = 0$ and the focusing effect is present only in the vertical plane. The corresponding tune shifts can be calculated by the formula:

$$\Delta\nu_y = \frac{1}{4\pi} \cdot \frac{B_y^2}{2(B\rho)^2} \beta_y L \left(1 + \frac{1}{12} \cdot \frac{L^2}{\beta_y} \right); \quad \Delta\nu_x = 0; \tag{3.2.12}$$

$$\left(\frac{\Delta\beta_y}{\beta_y} \right)_{\max} = \frac{2\pi \cdot \Delta\nu_y}{\sin(2\pi\nu_y)}; \quad \frac{\Delta\beta_x}{\beta_x} = 0; \tag{3.2.13}$$

The linear effects of IDs are proportional to the ratio $(B/E)^2$ (with B - magnetic field and E - beam energy) and to the averaged vertical beta at their locations. Therefore, the linear effects are more dominant in case of high field wigglers.

The main optical effects of CANDLE insertion devices (for single device) are summarized in Table 3.2.8.

Table 3.2.8 Main optical effects of IDs .

Insertion device	Wiggler I	Undulator I	Undulator II
$\rho_{ID} (m)$	5.05	14.3	33.3
ΔQ_y	0.063	0.032	0.0015
$\Delta\beta_y / \beta_y$ (%)	39.6	1.99	0.92

The parameters in Table 3.2.8 are the bending radius in insertion device ρ_{ID} , the linear vertical tune shift ΔQ_y and the maximum beta-beat $\Delta\beta / \beta$. Table 3.2.8 shows that the Wiggler I with the highest magnetic field of 1.98 T causes the main effects. In particular, the total tune shift drives the working point closer to the third order resonance line in resonance diagram. It also causes large value beta-beating. So, local correction of tunes and betatron function in case of operation of strong wiggler is mandatory. These effects are acceptable for the moderate field wiggler and undulator magnets.

As it was expected high field devices present stronger linear distortions than those with lower fields and shorter periods. In Fig.3.2.14 the modulated beta function produced by Wiggler I (which introduced comparatively big beta-beating) is shown in comparison with the bare lattice. Note, that the horizontal beta is un-effected by ID.

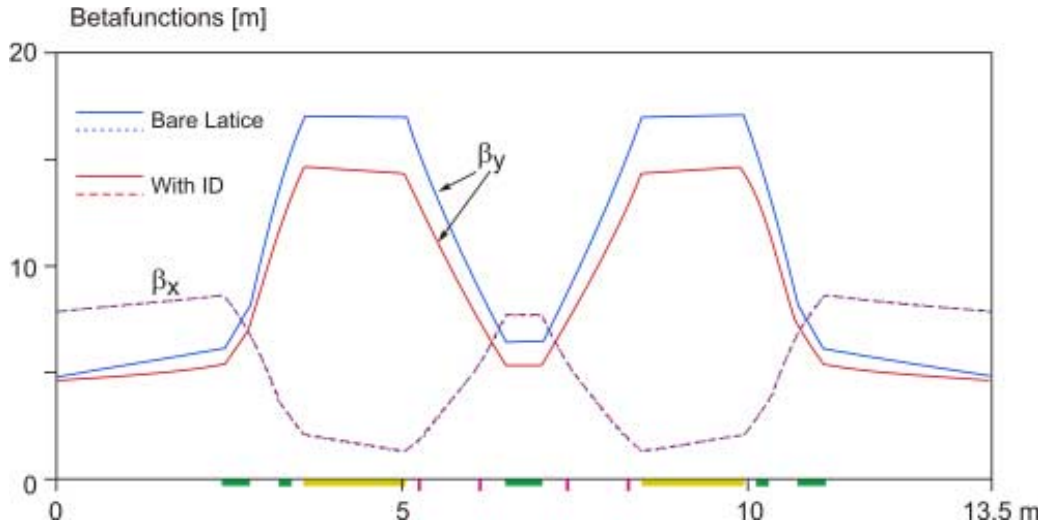


Fig. 3.2.14 Beta-beating for the storage ring lattice occupied by Wiggler I.

Synchrotron radiation and quantum excitation in wigglers increase the beam energy loss and change the equilibrium emittance and the beam energy spread. For the storage ring lattice without insertion devices the equilibrium emittance and the energy spread are:

$$\varepsilon_{x_0} = C_q \gamma^2 \cdot \frac{I_5}{I_2 - I_4}; \quad (3.2.14)$$

$$\sigma_{\varepsilon_0}^2 = C_q \gamma^2 \cdot \frac{I_3}{2I_2 + I_4}; \quad (3.2.15)$$

where $C_q = \frac{55}{32\sqrt{3}} \frac{\hbar}{mc} = 3.84 \cdot 10^{-13} m$; $\gamma=5871$ is Lorentz factor, I_k are the synchrotron integrals. In the presence of a single ID the formulas (3.2.14) and (3.2.15) are read as:

$$\varepsilon_x = \varepsilon_{x_0} \frac{1 + \frac{I_5^{ID}}{I_5^0}}{1 + \frac{I_2^{ID} - I_4^{ID}}{I_2^0 - I_4^0}}; \quad \sigma_{\varepsilon}^2 = \sigma_{\varepsilon_0}^2 \frac{1 + \frac{I_3^{ID}}{I_3^0}}{1 + \frac{2I_2^{ID} + I_4^{ID}}{2I_2^0 + I_4^0}}; \quad (3.2.16)$$

where the terms introduced by the ID are:

$$I_2^{ID} = \frac{\lambda N}{2\rho^2}; \quad I_3^{ID} = \frac{4\lambda N}{3\pi\rho^3}; \quad I_4^{ID} = -\frac{3\lambda^3 N}{32\pi\rho^4};$$

$$i_4^{ID} = \frac{7\lambda^2 \eta_0'}{9\pi^2 \rho^3}; \quad i_5^{ID} = \frac{4\lambda N}{3\pi\rho^3} [\gamma_0 \eta_0^2 + \beta_0 \eta_0'^2]; \quad (3.2.17)$$

$$I_5^{ID} = \frac{4\lambda N}{3\pi\rho^3} \frac{\eta_0^2}{\beta_0} + \frac{\lambda^3 N}{15\pi^3 \rho^5} \beta_0 + \frac{\lambda^5 N}{32\pi^5 \rho^5 \beta_0}.$$

The additional i_4^{ID} and i_5^{ID} terms correspond to the contributions arising from the small dispersion $\eta_0 = 0.18m$ in the straight sections.

The relative change of energy loss due to the radiation in the presence of insertion devices can be calculated by:

$$\frac{U - U_0}{U_0} = \frac{1}{2} \frac{L_{ID}}{2\pi\rho_0} \left(\frac{\rho_0}{\rho_{ID}}\right)^2; \quad (3.2.18)$$

where $\rho_0 = 7.385m$ is the radius of curvature in the main dipoles.

Table 3.2.9 lists the radiation effects of individual IDs. As it is seen from Table 3.2.9, the radiation effects of Undulator I and Undulator II on beam emittance and energy spread are positive. Wiggler I, in contrary, increases the emittance and the energy spread. In case of machine full occupation by undulators, the horizontal emittance is reduced from 8.4 nm-rad to 8.1 nm-rad .

Table 3.2.9 Main radiation effects of IDs.

Insertion device	Wiggler I	Undulator I	Undulator II
Relative energy loss $\frac{U - U_0}{U_0}$ (%)	9	0.46	0.21
Relative energy spread $\frac{\sigma_E - \sigma_E^0}{\sigma_E^0}$ (%)	0.16	-0.17	-0.11
Relative emittance change $\frac{\Delta\varepsilon_x}{\varepsilon_x}$ (%)	0.56	-0.21	-0.13

These conclusions are confirmed by Fig. 3.2.15, which shows the emittance behavior as a function of the insertion device field for Undulator I (a) and Wiggler I (b) magnets. The effect to energy spread is similar to the effect on the beam emittance. The change in energy spread depends on the ratio of the magnetic field in the insertion device to that in the bending magnet. Except for low fields, there is an increase in the beam energy spread (as shown in Fig. 3.2.16 for Undulator I (a) and Wiggler I (b) magnets.

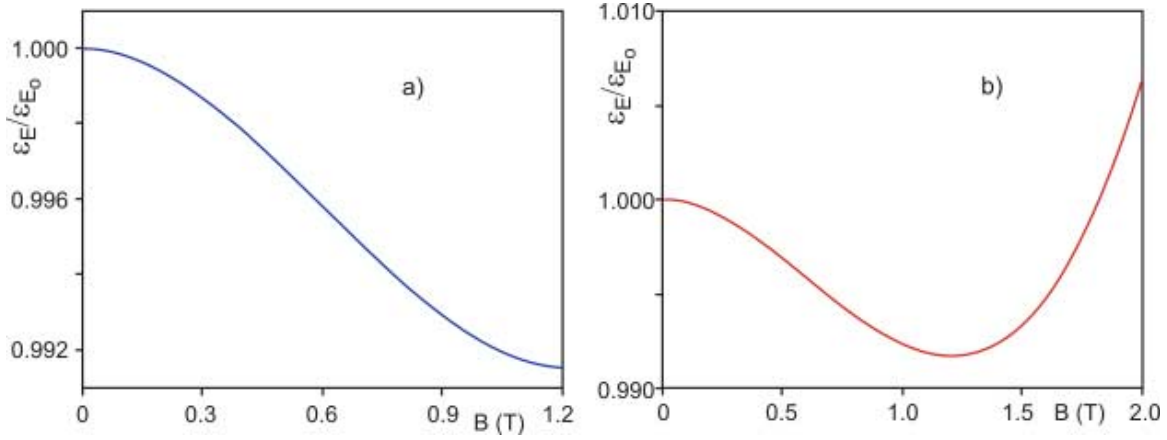


Fig. 3.2.15 Emittance dependence on the Undulator I (a) and Wiggler I (b) field.

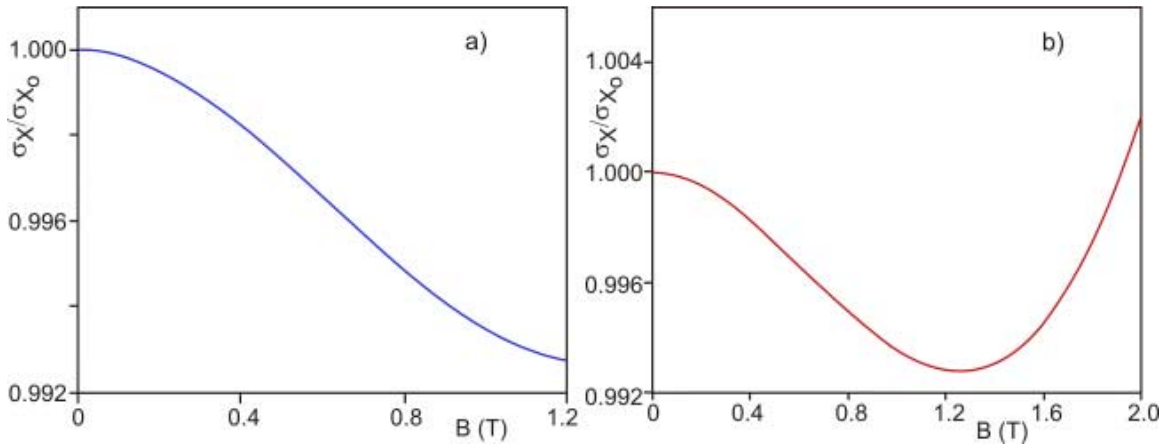


Fig.3.2.16 Energy spread dependence on Undulator I (a) and Wiggler I (b) field.

From the formula (3.2.16) one can obtain the condition under which beam emittance is unperturbed or is reduced [15]:

$$\lambda^2 \leq 5.87 \cdot 10^9 \frac{E \varepsilon_{x_0}}{B^3 < \beta >} ; \quad (3.2.19)$$

where E is beam energy in GeV and B is ID field in Tesla. The beam emittance is reduce if the period of the insertion device is below the value determined by the equation. For the IDs under consideration the transition point between the regions where emittance grows and where it reduces corresponds to the magnetic field value of $B_{ID} \approx 1.2T$.

Effects on dynamic aperture and lifetime.

The additional linear and non-linear effects applied by IDs may bring to the decrease of the dynamic aperture and affect the beam lifetime limiting. In Figure 3.2.15 the dynamic aperture simulations (vs sextupole aperture) obtained by computer code OPA are presented in case of bare lattice (solid line) and in case of Wiggler I in operation (dashed line). In computer code OPA the insertion device periodic field is implemented as a series of alternating sign dipole array:

$$\text{Undulator (one period)} \Rightarrow B^+ \ O \ B^- \ B^- \ O \ B^+$$

with the dipole field $B_D = B_0 \cdot \pi / 4$; the dipole length $L_D = \lambda_0 \cdot 4 / \pi^2$; and the distance between the poles $D = \lambda_0 / 2 - L_D$; where B_0 and λ_0 are the insertion device on-axis magnetic field and the period length respectively. This model provides very adequate beam trajectory and other optical characteristics. As Fig.3.2.17-18 show for the chosen planar devices the dynamic aperture reduction is observed only in periphery part of stability region.

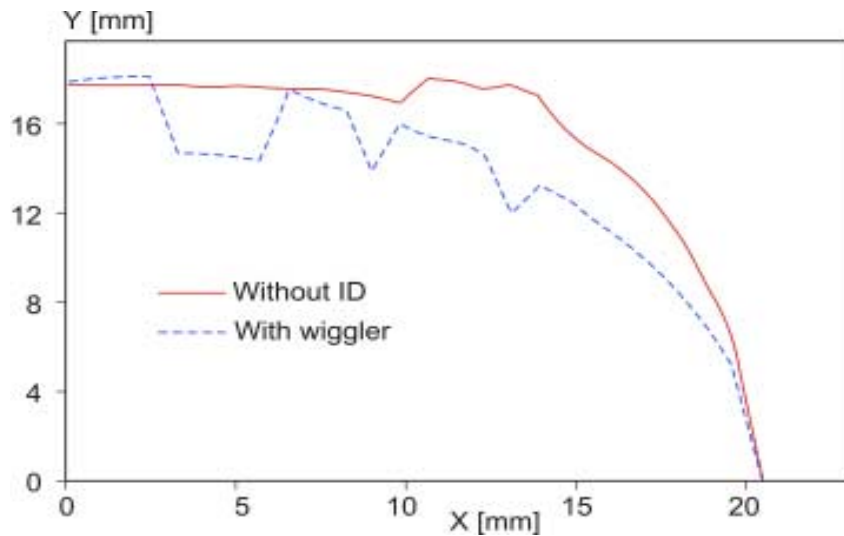


Fig.3.2.17. Dynamic aperture for the bare lattice (solid line) and including Wiggler I (dashed line).

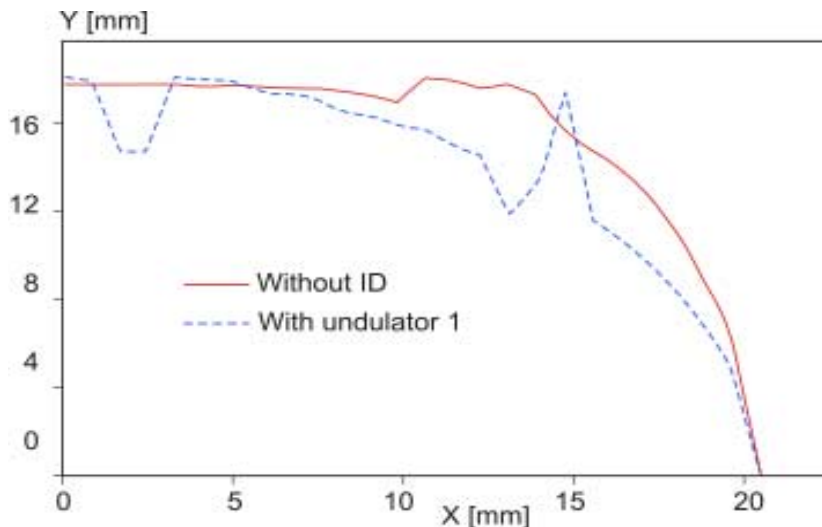


Fig.3.2.18. Dynamic aperture for the bare lattice (solid line) and including Undulator I (dashed line).

The above mentioned linear and non-linear fields of IDs will also produce beam lifetime limitations via reduction of dynamic aperture with couple of small gap. For the intermediate energy rings like CANDLE the Touschek lifetime limitation is dominant. In Fig. 3.2.19 the Touschek lifetime is plotted depending on longitudinal coordinate for the parameter value: total accelerating voltage 3.3 MV and 2.4% momentum acceptance assuming 1% emittance coupling. One can see the average Touschek lifetime reduction from 36.8 hour to 34.5 hour (one Wiggler I in operation). In the pessimistic scenario when all the straight sections are accommodated with the Wiggler I type insertion device the lifetime of the electron beam is reduced to 21 hours.

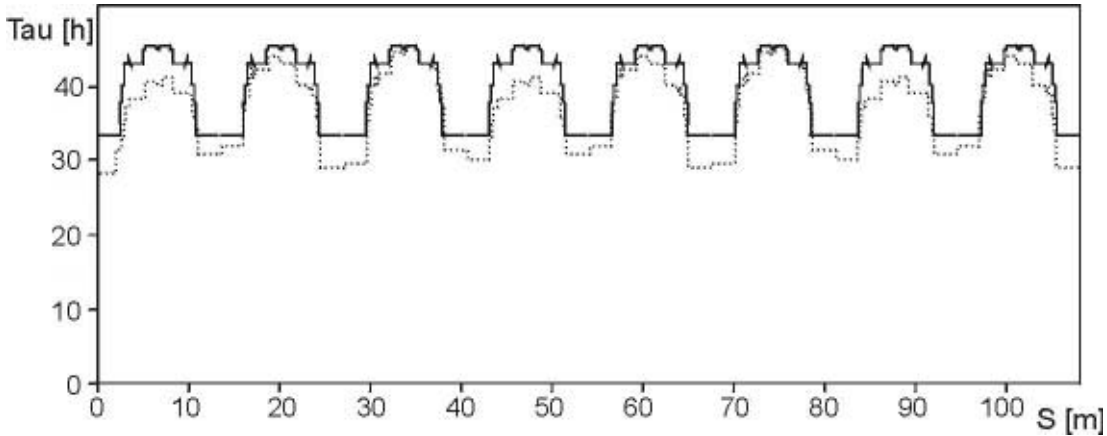


Fig. 3.2.19 Touschek lifetime vs longitudinal coordinate for bare lattice (solid line) and including Wiggler I (dashed line).

The simulations performed for the storage ring with the Undulator I and Undulator II in use show the comparatively small beam lifetime reductions. For the case when all the straight sections are loaded by insertion devices the maintenance of the sufficient Touschek lifetime of 27 hours will require the total accelerating voltage of 3.3 MV. The lifetime calculations have shown that the vertical gap of insertion devices less than 10 mm should then be possible with 350 mA beam current in multibunch mode and 3.3 MV total accelerating voltage.

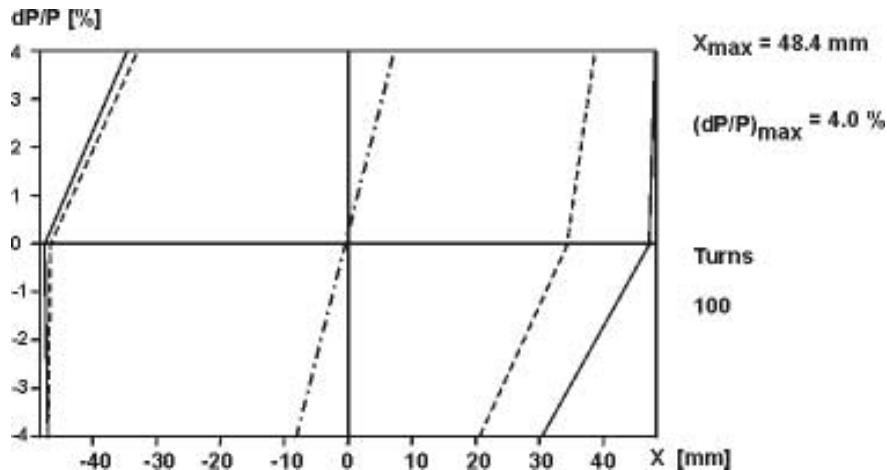


Fig. 3.2.20 Closed orbit distortion.

Fig. 3.2.20 presents the geometrical aperture (solid line), the closed orbit distortion (dot-and-dashed line) and the boundary of the horizontal dynamic aperture (dashed line) in the middle of the straight section with Wiggler I in operation. The comparison with the similar plot for bare lattice indicates no closed orbit distortion caused by insertion devices. The small closed orbit deviation in horizontal plane (Fig.3.2.20) is the result of small non-zero dispersion (0.18m) at the straight section.

3.2.6 Nonlinear Effects

Besides the linear terms, the equations of particle motion in real insertion devices contain also a nonlinear part the effect of which comes from an octupole-like term. In horizontal plane, the non-vanishing term is the oscillating field along the ID, the average contribution of which is zero. In the vertical plane the first non-linear wiggler effect comes from the octupole like field, which generate quadratically increasing vertical amplitude dependent tune shift:

$$\Delta Q_y^{oct} = \varepsilon_y \frac{\pi N \beta_y^2}{4 \lambda \rho^2} \left[1 + \frac{2}{3} \left(\frac{N \lambda}{2 \beta_y} \right)^2 + \frac{1}{5} \left(\frac{N \lambda}{2 \beta_y} \right)^4 \right]; \quad (3.2.20)$$

The non-linear effects are proportional to the ratio $(B/E\lambda)^2$ and therefore are more severe in case of small period undulator. Analytic calculations of the amplitude tune shifts for all three insertion devices have been performed. The results are presented in the Table 3.2.10 where we have taken $y = 5\text{mm}$, $\beta_y = 7.49\text{m}$ and $\varepsilon_y = 8.4 \cdot 10^{-2} \text{ nm}\cdot\text{rad}$.

Table 3.2.10 Nonlinear tune shifts from ID fields .

Insertion device	Wiggler I	Undulator I	Undulator II
$\Delta Q_y^{oct} [10^{-8}]$	3.73	11	1.0

As it is seen from Table 3.2.10, the nonlinear effects arising from octupole-like field of IDs are negligible due to very small vertical beam emittance in the storage ring.

It can be expected that non-linear fields can produce significant effects at large betatron amplitude. These betatron phase distortions break the periodicity of beta functions and the phase advance between sextupoles, which can lead to stronger sextupole resonances and reduction of dynamic aperture. The wiggler focusing effect should be compensated locally by utilizing four pairs of quadrupoles located symmetrically about the device.

In Fig. 3.2.21 and Fig. 3.2.22 the dynamic aperture reduction due to IDs non-linearities are presented as a result of direct symplectic integration of canonical equations of transverse motion.

The symplectic property of integration method as well as the stability criteria, were checked during the mapping by solving the linear system of 16 differential equations [16]

$$\dot{B} = A \cdot B; \quad (3.2.21)$$

where B is 4×4 matrix and A is 4×4 Jacobian matrix, associated with the canonical equations of motion.

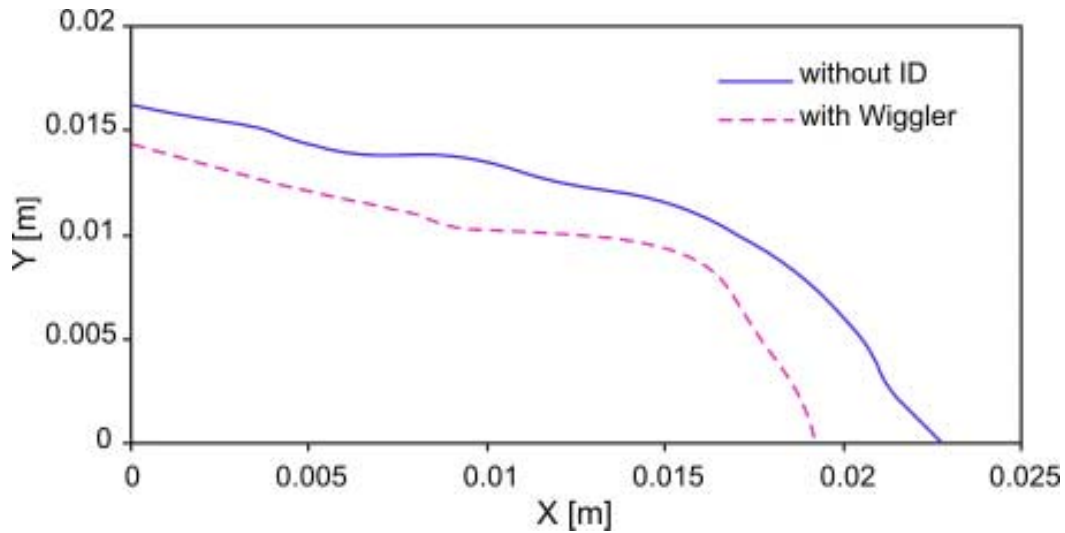


Fig. 3.2.21. Dynamic aperture reduction due to Wiggler operation.

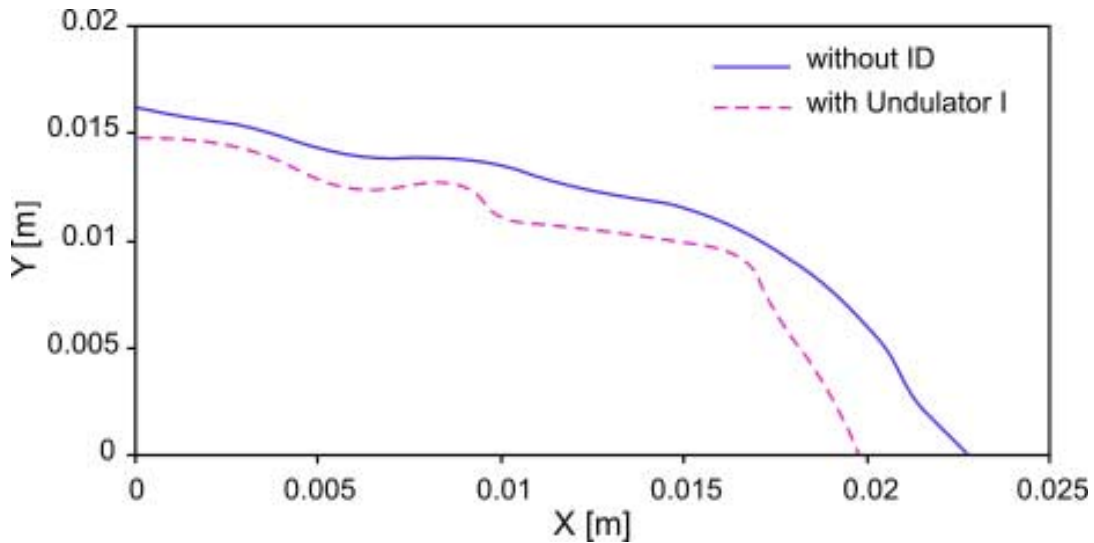


Fig. 3.2.22 Dynamic aperture reduction due to Undulator I operation.

The results of phase space calculations are presented in Fig. 3.2.23-25. Tracking simulations are carried out for the Gaussian bunch of 1001 particles with the initial standard deviations: $\sigma_x = 1.8\text{mm}$, $\sigma_x' = 0.8\text{mrad}$ and $\sigma_y = 0.7\text{mm}$, $\sigma_y' = 0.4\text{mrad}$. These values are taken more than twice as high as those for electron beam delivered from booster. Tracking results show the negligible influence to the beam dynamic aperture by the nonlinear field of storage ring main magnets. The dynamic amplitude reduction to 18mm in horizontal plane and 14.5mm in vertical plane are tolerable and still well outside the physical aperture of IDs in the middle of the straight section

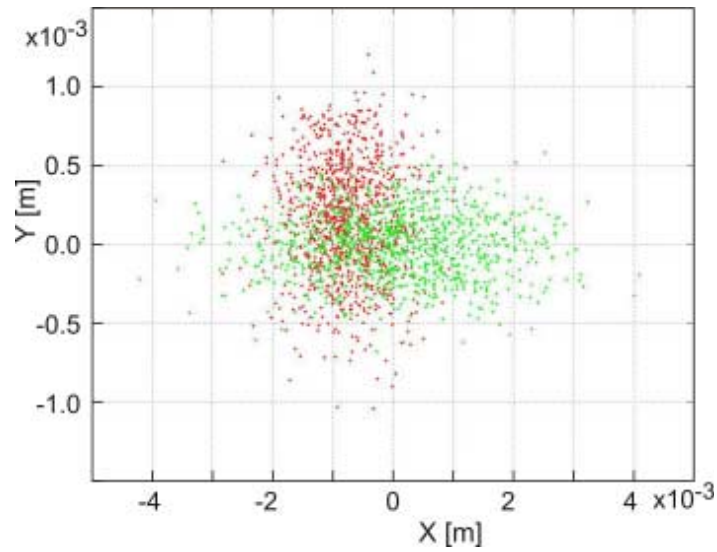


Fig. 3.2.23 Beam cross section evolution after one revolution around the ring.

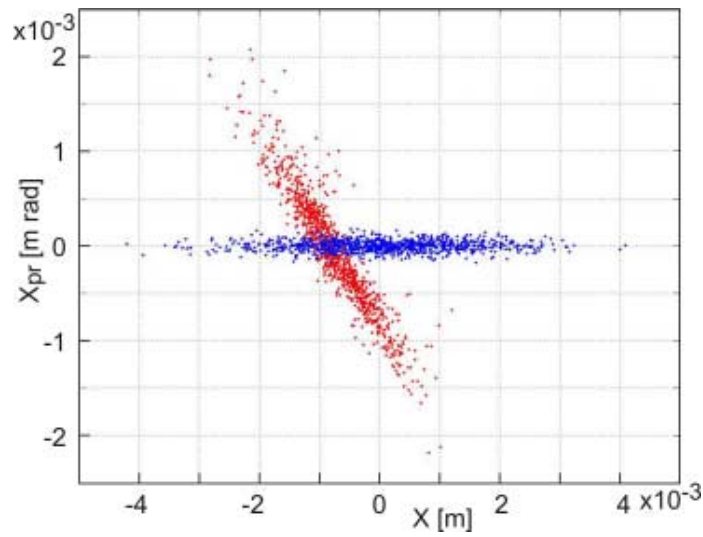


Fig 3.2.24 Horizontal phase space evolution after one revolution around the ring.

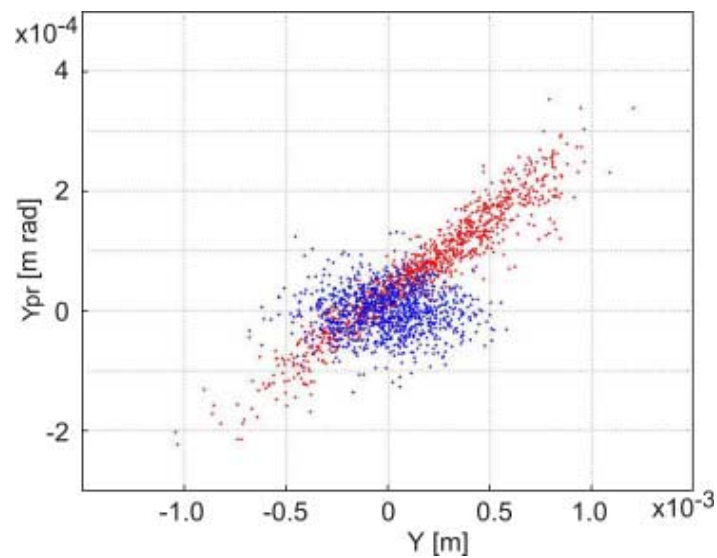


Fig 3.2.25 Vertical phase space evolution after one revolution around the ring.

The nonlinear chromaticity dependence of momentum spread is shown in Fig. 3.2.26. The horizontal lines $\xi_{x0} = -18.91$ and $\xi_{y0} = -14.87$ indicate the values of natural linear chromaticities in the horizontal and vertical planes respectively. The calculated values for the absolute bunch lengthening and the nonlinear term of momentum compaction factor are $\Delta\sigma_s = 0.00275mm$ and $\alpha_1 = 1.27 \cdot 10^{-5}$ respectively.

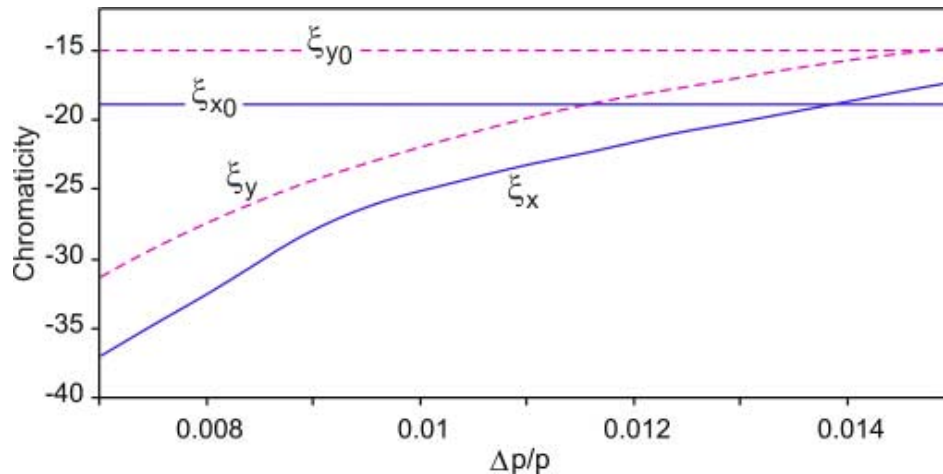


Fig 3.2.26 Nonlinear chromaticity vs momentum spread.

The more detailed study of nonlinear effects on the dynamic aperture reduction will be done using computer code RACETRACK [17].

Reference

1. H.L.Owen , MAD Version 8.23DL, DPG-XX-rpt-006, 2000,
2. Program POISSON, superfish@lanl.gov.
3. B.Autin and Y.Marti, "Closed Orbit Correction of A.G. Machines Using a Small Number of Magnets." CERN ISR-MA/73-17, Geneva, 1973.
4. H.Wiedemann, Particle Accelerator Physics I, Springer, 1999
5. A.Terebilo, "Accelerator Toolbox for MATLAB", SLAC-PUB-8732, 2001
6. 6.D.Sagan and D.Rubin "Linear Analysis of Coupled Lattices", Phys.Rev.ST,v.2,1999
7. D Edwards and L. Teng, "Parametrization of Linear Coupled Motion in Periodic Systems", IEEE Trans. Nucl.Sci. 20,3,1973
8. J.Corbett, A.Terebilo, "Interactive Orbit Control in MATLAB" SLAC-PUB- 8906, 2001
9. Tsakanov, V. et al , (2001), Armenian Light Source, CANDLE, these proceedings.
10. Martirosyan Y., Ivanyan M. and Tsakanov V., " Insertion Devices for the CANDLE Light Source", NATO ARW on "Electron-Photon Interaction in Dense Media", p.349, Nor-Hamberd, Armenia, 2001; Edited by H.Wiedemann.
11. Walker, R. and Diviacco, B.,(2000) Insertion Devices-Recent Developments and Future Trends, Synchrotron Radiation News, vol.13, #1.
12. Wrulich,A. (1999), Future Directions in the Storage Ring Development for Light Sources, Proc. of the PAC99, New York.
13. Smith, L Effects of Wigglers and Undulators on Beam Dynamics, LBL-ESG-24,1986.
14. Streun, A. (1997), OPA Documentation, PSI, Switzerland.
15. Ropert, A., (1996), Lattices and Emittances, CAS, Grenoble.
16. Dragt, A., "Lectures on Nonlinear Orbit Dynamics", AIP Conf. Proc. #87, R.Carrigan et al., (Eds.), 1982
17. Iazzourene, F. et al. RACETRACK User's Guide, ST/M-92/7, (1992).